

# Vertical structures induced by embedded moonlets in Saturn's rings: the gap region

H. Hoffmann\*, M. Seiß, F. Spahn

*Nonlinear Dynamics Group, Institute of Physics and Astronomy, University of Potsdam,  
14476 Golm, Germany*

---

## Abstract

We study the vertical extent of propeller structures in Saturn's rings. Our focus lies on the gap region of the propeller and on non-inclined propeller moonlets. In order to describe the vertical structure of propellers we extend the model of Spahn and Sremčević (2000) to include the vertical direction. We find that the gravitational interaction of ring particles with the non-inclined moonlet does not induce considerable vertical excursions of ring particles, but causes a considerable thermal motion in the ring plane. We expect ring particle collisions to partly convert the lateral induced thermal motion into vertical excursions of ring particles. For the gap region of the propeller, we calculate gap averaged propeller heights on the order of 0.7 Hill radii, which is of the order of the moonlet radius. In our model the propeller height decreases exponentially until viscous heating and collisional cooling balance. We estimate Hill radii of 370m and 615m for the propellers Earhart and Blériot. Our model predicts about 120km for the azimuthal extent of the Earhart propeller at Saturn's 2009 equinox, being consistent with values determined from Cassini images.

*Keywords:* Planetary rings, Saturn, Moonlets, Satellites, Dynamics, Disks

---

---

\*Corresponding author.

*Email address:* hohoff@uni-potsdam.de (H. Hoffmann)

## 1. Introduction

Planetary rings are one of the most remarkable and beautiful cosmic structures. They are considered to be natural dynamical laboratories (Burns and Cuzzi, 2006), exemplifying the physics of cosmic disks, such as accretion disks or galactic disks, which are much larger and much farther away from Earth. An exciting example is the presence of small moons embedded in Saturn's rings, henceforth called moonlets, which have their analog in planetary embryos orbiting within a protoplanetary disk (Artymowicz, 2006; Papaloizou et al., 2007).

The fact that the resolution of even *Cassini's* cameras is too low to image these moonlets directly, brought up the idea of investigating moonlet induced putative structures in the rings (Spahn, 1987; Spahn and Wiebicke, 1989), with the hope that these features could be captured by the spacecraft cameras or instruments. This then led to predictions of the propeller structures (Spahn and Sremčević, 2000; Sremčević, Spahn, and Duschl, 2002) which are carved in the rings by the moonlet. Subsequent numerical particle experiments (Seiß et al., 2005; Sremčević et al., 2007; Lewis and Stewart, 2009) completed the *fingerprint* of such gravitational perturbers and confirmed the spatial scaling of the propeller structure. Depending on its size, an embedded ring-moon either creates a propeller (sizes below 1 km) or, alternatively, opens up a circumferential gap (for sizes  $> 1$  km, e.g. the ring-moons *Pan* and *Daphnis*). Both structures, propeller and circumferential gap, are decorated with density wakes, completing the structural picture. Up to this stage, all these density features have been assumed to occur only in the ring plane, a vertical stratification of moonlet induced structures has not seemed to be of importance.

More than 150 propeller moonlets have now been detected (Tiscareno et al., 2006, 2008) and among them a few which are large enough to allow *Cassini's* cameras to take several snapshots of their propellers at different times, confirming in this way their orbital motion. Those moonlets were nicknamed after famous aviators, e.g.: Blériot, Kingsford Smith, Earhart (Tiscareno et al., 2010).

In the summer of 2009, at Saturn's equinox (the Sunset at Saturn's rings),

the perfect opportunity arose to detect any vertical structure deviating from the mean ring plane by observing shadows cast on the rings. At this time the density structures around the largest propeller moonlets, as well as those around the ring-moon *Daphnis*, created prominent shadows. These can be assigned to the wakes and in the case of the propeller moonlets also to excited regions of the propeller, where the moonlet induces a partial gap. The shadows were much longer than the moon's size itself. The lateral extent of the shadows allows to conclude that moonlet induced vertical excursions of ring particles can be in the range of several kilometers in the case of *Daphnis* or several hundred meters in the case of the large propeller moonlets. These very facts directly indicate the necessity to investigate the vertical stratification of moonlet induced structures, which has not been the focus of former models of the moonlet's *fingerprint*. In this work we will study the vertical extent of moonlet induced propeller structures, focusing on the gap region of the propeller.

The paper is organized as follows: In Section 2 the extended propeller model is presented. In Section 2.2 the mass flow through the scattering region is calculated by a probabilistic approach, and values of the moonlet induced thermal velocities are determined, which are later used as initial conditions for the hydrodynamical equations. Section 2.3 gives the hydrodynamical balance equations, which we use to model the diffusion of mass into the induced gap and the relaxation of the ring temperature. In Section 3 we calculate the height of the ring in the gap region of a propeller. Section 4 discusses made assumptions and the application of our results to propeller features in Saturn's rings. Our results are summarized in Section 5.

## 2. Extended model of gravitational scattering

### 2.1. The scattering region

The first step in the formulation of our model, is to divide the planetary ring, composed of granular grains and one moonlet, into two regions:

- (i) the scattering region,

(ii) the rest of the ring.

In this work we consider moonlets on circular, i.e. on non-inclined and non-eccentric, orbits. The scattering region is the small area (volume) around the moonlet where the majority of the trajectory changes, due to the moonlet's gravity, take place. This region of the embedded moonlet's gravitational influence is of the order of a few Hill radii

$$h = a_0 \left( \frac{m_m}{3(m_m + m_s)} \right)^{1/3}, \quad (1)$$

where  $a_0$  is the semimajor axis of the moonlet,  $m_m$  its mass and  $m_s$  the mass of Saturn. Compared to the moonlet's semimajor axis the Hill radius is usually very small. For large propeller moonlets, like Blériot or Earhart, the ratio  $h^* = h/a_0$  is approximately  $10^{-6}$  (Tiscareno et al., 2010). This low ratio naturally allows the splitting of the rings into the two regions, where the scattering region is shrunk to a line.

For the rest of the ring, where the moonlet's gravity is negligible, the moonlet induced structures are assumed to relax due to inelastic collisional cooling and viscous diffusion (Spahn and Sremčević, 2000; Sremčević, Spahn, and Duschl, 2002). In previous hydrodynamic models the former process, the relaxation of the granular temperature  $T \sim c^2/3$ , has not been considered. This thermal relaxation and 3D-scattering are the major themes of this work.

## 2.2. Encounter with the moonlet – gravitational scattering

We describe the encounter of ring particles with the moonlet in a corotating frame, rotating about Saturn with the mean motion of the moonlet. The frame's origin coincides with the mean orbital location of the moonlet. The x axis points radially outward, the y axis points into the azimuthal direction and the z axis is normal to the ring plane in a way that the axes form a right handed coordinate system.

With this, the dynamics of ring particles in the corotating frame is given by

$$\ddot{\mathbf{r}} + 2\boldsymbol{\Omega}_0 \times \dot{\mathbf{r}} + \boldsymbol{\Omega}_0 \times (\boldsymbol{\Omega}_0 \times \mathbf{r}) = -\nabla\Phi_s - \nabla\Phi_m, \quad (2)$$

where  $\Phi_s$  and  $\Phi_m$  are the gravitational potentials due to Saturn and the moonlet.

The ring particles are on orbits with low eccentricity and inclination and the mass of the moonlet is very small compared to Saturn's mass  $m_m/m_s \ll 1$ . In the vicinity of the moonlet the equations of motion of ring particles are well approximated by Hill's equations (Hill, 1878; Hénon and Petit, 1986).

With the scaled coordinates  $\tilde{x} = x/h$ ,  $\tilde{y} = y/h$ ,  $\tilde{z} = z/h$  and scaled time  $t' = \Omega_0 t$  Hill's equations become

$$\begin{aligned}\ddot{\tilde{x}} &= 2\dot{\tilde{y}} + 3\tilde{x} - 3\tilde{x}/\tilde{s}^3 \\ \ddot{\tilde{y}} &= -2\dot{\tilde{x}} - 3\tilde{y}/\tilde{s}^3 \\ \ddot{\tilde{z}} &= -\tilde{z} - 3\tilde{z}/\tilde{s}^3 ,\end{aligned}\tag{3}$$

where  $\tilde{s}^2 = \tilde{x}^2 + \tilde{y}^2 + \tilde{z}^2$  is the scaled distance to the moonlet and  $\dot{\tilde{x}} = d\tilde{x}/dt'$ . These equations are point symmetric about the position of the moonlet ( $\tilde{x} = \tilde{y} = \tilde{z} = 0$ ), and quite comfortable, they do not depend on the moonlet mass anymore. All information of the moonlet mass is contained in the scaling length  $h$ .

When the ring particles are not in the vicinity of the moonlet, i.e.  $1/\tilde{s}^3 \rightarrow 0$  and therefore  $|\nabla\Phi_s| \rightarrow 0$ , their trajectories are well described by the solutions to the homogeneous Hill's equations

$$\begin{aligned}\tilde{x}(t') &= \tilde{a} - \tilde{e} \cos(t' + \tilde{\tau}) \\ \tilde{y}(t') &= C - \frac{3}{2}\tilde{a}t' + 2\tilde{e} \sin(t' + \tilde{\tau}) \\ \tilde{z}(t') &= \tilde{i} \sin(t' + \tilde{\omega}) .\end{aligned}\tag{4}$$

The semimajor axis, eccentricity and inclination are scaled according to

$$\tilde{a} = \frac{a - a_0}{h}, \quad \tilde{e} = \frac{ea_0}{h}, \quad \tilde{i} = \frac{ia_0}{h} ,\tag{5}$$

where a spherically symmetric planet ( $\Phi_s \sim -Gm_s/r$ ) is assumed. The phases  $\tilde{\tau}$  and  $\tilde{\omega}$  are the longitude of pericenter and the longitude of the ascending node respectively.

### 2.2.1. Test particle integrations

We integrate the equations of motion numerically for a set of test particles using a 5th order embedded Runge-Kutta scheme with adaptive step size control (Press et al., 1992). The moonlet and Saturn are assumed to be point masses. The integrations start upstream of the moonlet at an azimuthal distance of 1000 Hill radii to the moonlet and are terminated when the test particle’s azimuthal distance exceeds 1000 Hill radii. These limits ensure that the region of interaction is well included in the integration.

We take the initial semimajor axis of the test particles to be uniformly distributed in the range of  $-20$  to  $20$  Hill radii radial distance to the moonlet. The initial eccentricities and inclinations of the test particles are chosen to be Rayleigh distributed

$$f(\tilde{e}, \tilde{i}) = \frac{\tilde{e}}{\tilde{c}_x^2} \exp\left(-\frac{\tilde{e}^2}{2\tilde{c}_x^2}\right) \frac{\tilde{i}}{\tilde{c}_z^2} \exp\left(-\frac{\tilde{i}^2}{2\tilde{c}_z^2}\right) \quad , \quad (6)$$

with uniformly distributed initial phases  $\psi$  and  $\zeta$ . This is a fair assumption for many kinds of disks (Petit and Hénon, 1987; Ida and Makino, 1992; Lissauer, 1993; Ohtsuki and Emori, 2000).

This distribution of orbital elements corresponds to a triaxial Gaussian velocity distribution

$$f(\tilde{v}_x, \tilde{v}_y, \tilde{v}_z) = \frac{1}{\pi\tilde{c}_x^2} \exp\left(-\frac{\tilde{v}_x^2 + 4\tilde{v}_y^2}{\tilde{c}_x^2}\right) \frac{1}{\sqrt{2\pi\tilde{c}_z^2}} \exp\left(-\frac{\tilde{v}_z^2}{\tilde{c}_z^2}\right) \quad (7)$$

with a diagonal velocity dispersion tensor  $\mathbf{T}$ , where  $T_{xx} = \tilde{c}_x^2$ ,  $T_{yy} = (\tilde{c}_x/2)^2$  and  $T_{zz} = \tilde{c}_z^2$ . The scaled quantities  $\tilde{c}_x$ ,  $\tilde{c}_z$  are related to the unscaled ones by

$$\tilde{c}_x = c_x/(\Omega_0 h), \quad \tilde{c}_z = c_z/(\Omega_0 h). \quad (8)$$

We choose the ratio  $\tilde{c}_z/\tilde{c}_x = 0.65$ , which is consistent with the above Gaussian velocity distribution (Goldreich and Tremaine, 1978) and which is a reasonable value if we neglect self gravity (Salo et al., 2001).

This deviation from the Maxwellian velocity distribution of conservative gases is an expression of the non-equilibrium state, caused by the steady dissipation of orbital energy in collisions. This energy loss is counterbalanced by the

energy gain due to viscous Keplerian shear, guaranteeing a quasi-equilibrium manifested by a steady state. This energy pumping goes at the expense of the collective Keplerian motion and thus the ring particles spiral slowly into Saturn in the long term ( $10^8$  years).

During the trajectory integrations, the test particles and the moonlet are assumed to be point masses and the minimal distance of the test particles to the moonlet is recorded. For simplicity, we ignored particles which would collide with a spherical moonlet of finite size in further calculations. To estimate the difference, we also examined the case where all particles are used. Although the radial position of the maximally induced ring temperature changes a bit, we found no significant changes in the resulting gap averaged heights.

### 2.2.2. Mass transfer

We use the approach of Spahn and Wiebicke (1989) to describe the mass transfer through the scattering region. Motivated by the chaotic behaviour of single particle trajectories near the moonlet (Petit and Hénon, 1986), the encounter of ring particles with the moonlet is modelled by a probabilistic Markov chain model. The results of the test particle integrations are used to calculate transitional probabilities between initial  $(\tilde{x}, \tilde{z})$  and final  $(\tilde{x}', \tilde{z}')$  positions of the test particles at the azimuthal boundary of the scattering region. These probabilities define a scattering operator  $A$ , where  $A(\tilde{x}', \tilde{z}' | \tilde{x}, \tilde{z}) d\tilde{x} d\tilde{z}$  is the probability that matter is scattered from  $(\tilde{x}, \tilde{x} + d\tilde{x}) \times (\tilde{z}, \tilde{z} + d\tilde{z})$  to  $(\tilde{x}', \tilde{x}' + d\tilde{x}') \times (\tilde{z}', \tilde{z}' + d\tilde{z}')$ . The primes denote values after the scattering.

We assume that the scattering region can be approximated by the  $\tilde{x}$ - $\tilde{z}$  plane at  $\tilde{y} = 0$ , which connects Saturn and the moonlet and is analogous to the scattering line of Spahn and Wiebicke (1989). In our model, the complete action of the moonlet on the ring particles happens at this scattering plane. The scattering operator relates the azimuthal mass flux entering the scattering region to the azimuthal mass flux leaving the scattering region

$$|J_{\tilde{y}}(\tilde{x}', \tilde{y} = 0^\pm, \tilde{z}')| = \iint d\tilde{x} d\tilde{z} A(\tilde{x}', \tilde{z}' | \tilde{x}, \tilde{z}) |J_{\tilde{y}}(\tilde{x}, \tilde{z}, \tilde{y} = 0^\mp)| . \quad (9)$$

Mass conservation is expressed as a condition for the scattering operator

$$\iint d\tilde{x}' d\tilde{z}' A(\tilde{x}', \tilde{z}' | \tilde{x}, \tilde{z}) = 1 , \quad (10)$$

also illustrating that accreting particles are ignored here.

For the numerical calculation of the scattering operator we divide the radial and the vertical direction into bins. The bin  $(j, k)$  describes the region  $(\tilde{x}_j, \tilde{x}_{j+1}) \times (\tilde{z}_k, \tilde{z}_{k+1})$ ,  $j$  being an index in radial direction and  $k$  one in vertical direction. In the following, primed bin indices refer to the situation after the scattering by the moonlet and unprimed ones to the situation before.

The discretized scattering operator is then calculated by

$$A(j', k' | j, k) = \frac{N(j', k', j, k)}{N(j, k)} , \quad (11)$$

where  $N(j, k)$  is the number of test particles starting in bin  $(j, k)$ . We use an averaging procedure to calculate the number of test particles  $N(j', k', j, k)$  starting in bin  $(j, k)$  and ending in bin  $(j', k')$ . For each radial end bin  $j'$ , describing the interval  $(\tilde{x}_{j'}, \tilde{x}_{j'+1})$ , the time per orbit, the test particle will stay in this radial end bin is calculated (Spahn, 1987)

$$p(j') = \frac{\Delta t(j')}{T} = \frac{1}{\pi} \left| \arccos \left( \frac{\tilde{a} - \tilde{x}_{j'+1}}{\tilde{e}} \right) - \arccos \left( \frac{\tilde{a} - \tilde{x}_{j'}}{\tilde{e}} \right) \right| . \quad (12)$$

$N(j', k', j, k)$  is then calculated by

$$N(j', k', j, k) = \sum_n p^{(n)}(j') \delta^{(n)}(k') \delta^{(n)}(j, k) , \quad (13)$$

where the sum is over all test particles and  $\delta^{(n)}(j, k)$  is 1 for test particles starting in bin  $(j, k)$  and 0 otherwise.

Outside the scattering region we describe the ring using hydrodynamical equations. We assume that the fluid parcels entering and leaving the scattering region have a Keplerian azimuthal mean velocity  $\tilde{u}_{\tilde{y}}(\tilde{x}) = -3\tilde{x}/2$ . The azimuthal mass flux at the scattering plane is then (Spahn and Wiebicke, 1989)

$$J_{\tilde{y}}(\tilde{x}, \tilde{y} = 0^\pm, \tilde{z}) = \rho(\tilde{x}, \tilde{y} = 0^\pm, \tilde{z}) \tilde{u}_{\tilde{y}}(\tilde{x}) , \quad (14)$$

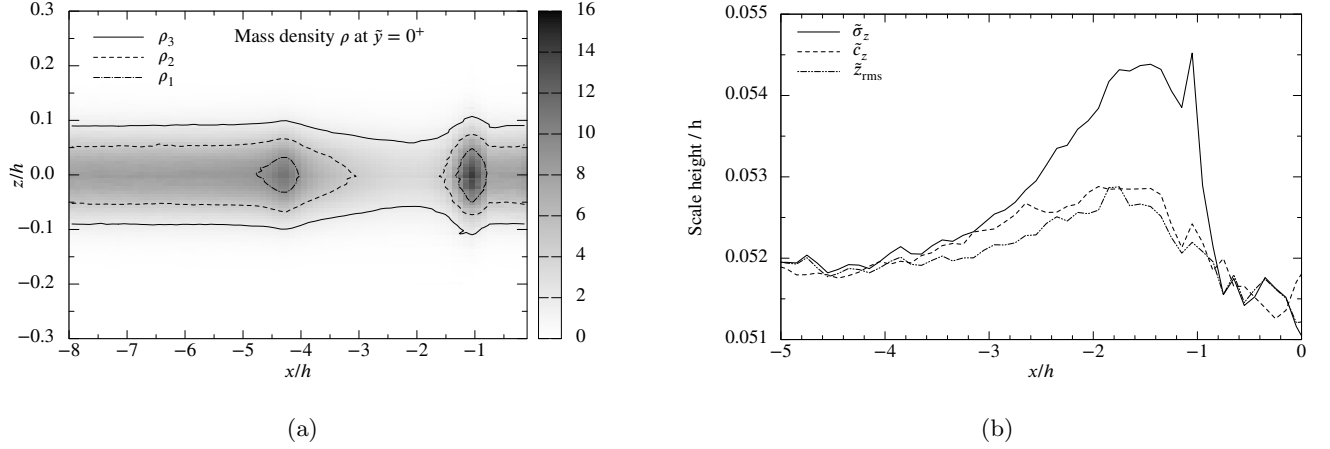


Figure 1: (a) Mass density  $\rho$  scaled by  $\Sigma_0/h$  after scattering by a moonlet with a Hill radius of 300m. The contour lines are for  $\rho_1 = 1.15 \rho_0(\tilde{z} = 0)$ ,  $\rho_2 = \rho_0(\tilde{z} = \tilde{c}_z)$  and  $\rho_3 = \rho_0(\tilde{z} = \sqrt{3}\tilde{c}_z)$ , where  $\rho_0$ , given by equation (16), is the mass density before the scattering by the moonlet. Clearly seen is the less dense gap region between  $1.5 \leq |\tilde{x}| \leq 4$ . (b) Ring thickness after the scattering by the same moonlet measured by: standard deviation  $\tilde{\sigma}_z$  of the vertical mass density profile, root mean square  $\tilde{z}_{\text{rms}}$  of the vertical excursions and vertical thermal velocity  $\tilde{c}_z$ , all at  $\tilde{y} = 0^+$ . All three are within a few percent of the values before the scattering by the moonlet, illustrating that the moonlet's gravity alone does not induce considerable vertical excursions of ring particles.

where  $\rho$  denotes the mass density. The mass transfer through the scattering region is thus calculated by

$$\rho(j', k') = \frac{1}{|\tilde{u}_{\tilde{y}}(j')|} \sum_{j,k} A(j', k' | j, k) \rho(j, k) |\tilde{u}_{\tilde{y}}(j)| . \quad (15)$$

We assume the ring to be in an equilibrium state before the encounter with the moonlet. In the following all quantities of the unperturbed ring have the subscript 0. The surface mass density  $\Sigma_0$  shall be constant, so that the mass density in the thin-disk approximation is given by

$$\rho_0(\tilde{x}, \tilde{y}, \tilde{z}) = \frac{\Sigma_0/h}{\sqrt{2\pi\tilde{c}_{z0}^2}} \exp\left(-\frac{\tilde{z}^2}{2\tilde{c}_{z0}^2}\right) . \quad (16)$$

The two plots in Figure 1 are made for a moonlet with 300m Hill radius and the orbital parameters of Earhart (Tiscareno et al., 2010). We have chosen the

velocity dispersion of the unperturbed ring to be  $c_0 = 3.9\text{mm/s}$ , corresponding to  $\tilde{c}_z = 0.052$ . Because of the point symmetry of the Hill equations (3), we show only values for  $\tilde{x} \leq 0$  in the plots.

Figure 1a shows the mass density  $\rho$  scaled by  $\Sigma_0/h$  after the scattering by the moonlet. The mass density in the regions  $|\tilde{x}| < 1$  and  $|\tilde{x}| > 5$  is nearly unchanged, whereas the gap region  $1.5 < |\tilde{x}| < 4$  has a considerably lower mass density than the ring before the scattering by the moonlet. There are two regions of high mass density around  $|\tilde{x}| = 1$  and  $|\tilde{x}| = 4.25$ . The solid line ( $\phi = 0.0$ ) in Figure 3b shows the corresponding surface mass density.

Also shown are three contour lines, corresponding to characteristic values of the unperturbed mass density  $\rho_0$  given by equation (16). The first contour line is for  $\rho_1 = 1.15 \cdot \rho_0(\tilde{z} = 0)$ , i.e. 15 percent larger than the maximal value of  $\rho_0$ . The second contour line is for the mass density value  $\rho_2 = \rho_0(\tilde{z} = \tilde{c}_{z0})$ . For low optical depths  $\tilde{c}_z$  is a good estimate of  $\tilde{z}_{\text{rms}}$ , the root mean square value of the vertical excursion of the ring particles. The third contour line shows the mass density  $\rho_3 = \rho_0(\tilde{z} = \sqrt{3}\tilde{c}_{z0})$ , where  $z = \sqrt{3}\tilde{c}_z$  is half of the effective geometric thickness of the ring. The effective geometric thickness  $H_{\text{eff}} = \sqrt{12}\tilde{z}_{\text{rms}} \approx \sqrt{12}\tilde{c}_z$  of the ring corresponds to the width of a uniform vertical mass density profile with the same standard deviation as a Gaussian one.

Figure 1b shows different measures of the ring thickness after the scattering by the moonlet. To calculate the ring thickness from the mass density, we consider the mass in bin  $(j', k')$  divided by the total mass in bins with bin index  $j'$

$$q(j', k') = \frac{\rho(j', k')}{\sum_{k'} \rho(j', k')}, \quad (17)$$

where we assumed uniform bin sizes. As a quantity,  $q$  describes the distribution of mass in the vertical direction and formally behaves like a probability, i.e.  $0 \leq q(j', k') \leq 1$  and  $\sum_{k'} q(j', k') = 1$ . The vertical displacement of the ring plane from  $\tilde{z} = 0$ , calculated from the mass density, is then given by

$$\tilde{\mu}_{z,j'} = \sum_{k'} \tilde{z}_{k'} q(j', k'), \quad (18)$$

with  $\bar{z}_{k'}$  being the midpoint of the vertical interval  $(\tilde{z}_{k'}, \tilde{z}_{k'+1})$ . The scale height of the ring is then proportional to

$$\tilde{\sigma}_z(j') = \left( \sum_{k'} (\bar{z}_{k'} - \tilde{\mu}_{z,j'})^2 q(j', k') \right)^{1/2}. \quad (19)$$

We also calculated the root mean square value of the vertical excursion of ring particles directly from the results of test particle integrations. With the averaging procedure of equation (12)  $\tilde{z}_{\text{rms}}$  is given by

$$\tilde{z}_{\text{rms},j'} = \left( \frac{\sum_n p^{(n)}(j') [\tilde{z}^{(n)} - \langle \tilde{z} \rangle_{j'}]^2}{\sum_n p^{(n)}(j')} \right)^{1/2}, \quad (20)$$

with

$$\langle \tilde{z} \rangle_{j'} = \frac{\sum_n \tilde{z}^{(n)} p^{(n)}(j')}{\sum_n p^{(n)}(j')}. \quad (21)$$

For the unperturbed mass density  $\rho_0$ , both  $\tilde{\sigma}_{z0}$  and  $\tilde{z}_{\text{rms}0}$  equal  $\tilde{c}_{z0}$ . The values after the scattering by the moonlet shown in Figure 1b are within 6 percent of the values of the unperturbed ring. Calculations for moonlets with different Hill radii from 50m to 500m confirm that the difference of the unperturbed values to the ones after the scattering by the moonlet are small, e.g. a few percent.

Up to now we have only considered the gravitational interaction with the moonlet. Thus, the values of  $\tilde{\sigma}_z$ , determined from the mass density  $\rho$ , and of  $\tilde{z}_{\text{rms}}$ , the root mean square of the test particle's vertical excursions, are the result of gravitational excitement only. The increase of a few percent of these values can not explain the height of propeller structures as inferred from their shadow length. A picture which changes drastically if a moonlet on an inclined orbit is considered, which is an issue of ongoing future work.

Because the moonlet does not induce considerable vertical excursions of ring particles, we restrict, in the following, our description to the ring plane and model the vertical propeller structure by the granular ring temperature  $T = (\tilde{c}_x^2 + \tilde{c}_y^2 + \tilde{c}_z^2)/3$ .

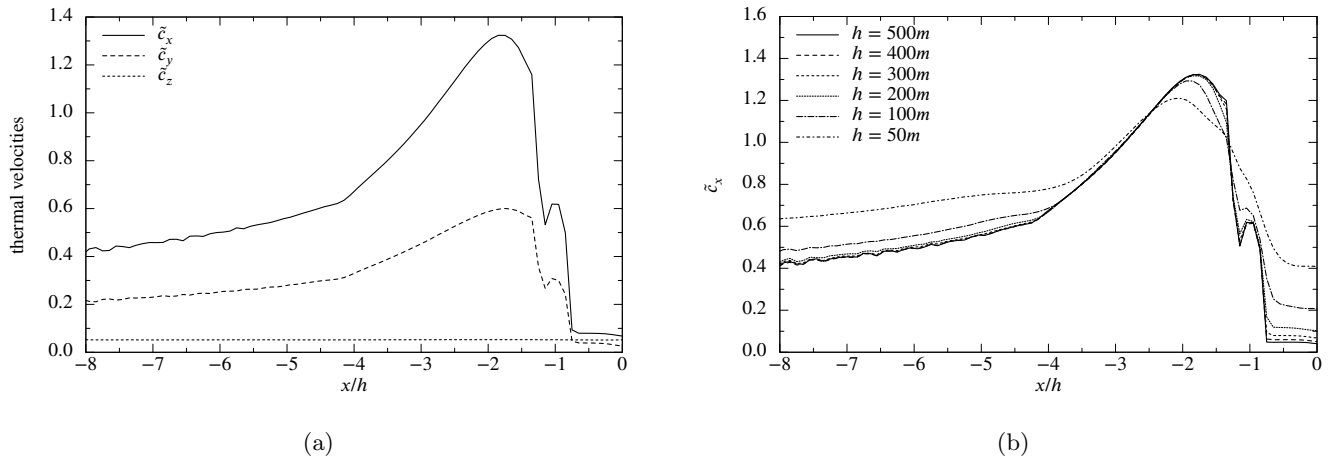


Figure 2: Moonlet induced thermal velocities as functions of the radial coordinate  $\tilde{x}$  at  $\tilde{y} = 0^+$ . All thermal velocities are scaled by  $\Omega_0 h$ . (a) Thermal velocities after the gravitational scattering by a moonlet with 300m Hill radius. The moonlet induces much more thermal motion in the ring plane than in vertical direction. (b) Comparison of the radial thermal velocity  $\tilde{c}_x$  after the scattering by moonlets with different Hill radii. In the gap region  $-4 \leq \tilde{x} \leq -1.5$  the radial thermal velocity scales well with  $\Omega_0 h$  for the larger moonlets ( $h = 100m$  and above).

### 2.2.3. Velocity dispersion

In this subsection we determine values of the moonlet induced thermal velocities after the scattering by the moonlet, which are later used as initial conditions for the hydrodynamical equations. We assume that after the scattering by the moonlet, the particles are on Keplerian orbits which are well described by equation (4). We calculate the thermal speed components  $\tilde{c}_x$ ,  $\tilde{c}_y$  and  $\tilde{c}_z$  by taking the weighted sample standard deviation of  $\tilde{v}_x$ ,  $\tilde{v}_y - 3\tilde{x}/2$  and  $\tilde{v}_z$  for the set of integrated test particles. For  $\tilde{c}_x$  for example

$$\tilde{c}_x(j') = \left( \frac{\sum_n p^{(n)}(j') [\tilde{v}_x^{(n)} - \langle \tilde{v}_x \rangle(j')]^2}{\sum_n p^{(n)}(j')} \right)^{1/2}, \quad (22)$$

where  $j'$  denotes the radial bin number.

Due to the averaging process (12) our model does not describe moonlet wakes, which are moonlet induced coherent motions of ring particles (Showalter et al., 1986; Spahn, Scholl and Hertzsch, 1994). Nevertheless our model describes the gap region quite well, because test particles ending in this region are often on trajectories which are very sensitive to initial conditions (Hénon and Petit, 1986), and their phases are mixed up. Furthermore, wake structures start to dissolve when nearby streamlines cross. For the gap region this happens very fast, i.e. for the middle of the gap at  $|\tilde{x}| = 2.5$  after 0.4 orbits.

For the region beyond the gap however, we have to keep in mind that we might overestimate  $\tilde{c}_x$  and  $\tilde{c}_y$  with equation (22). The averaging process destroys the coherent phase relations and systematic motion looks partly like thermal motion. In this work we focus on the moonlet induced gap, which is important on its own, because of the large thermal excitation in the gap region (cf. Figure 2).

The values of the mean thermal velocities, calculated with equation (22), are the result of the gravitational interaction with the moonlet only. Figure 1b shows  $\tilde{c}_z$  and  $\tilde{z}_{\text{rms}}$ , which do not deviate much at  $\tilde{y} = 0^+$ . In Figure 2a we compare the mean thermal velocities after the scattering by the moonlet of Figure 1. The maximum excitement in each case lies near the inner edge of the

moonlet induced gap at a radial position of about  $|\tilde{x}| = 7/4$ .

The moonlet induces much more thermal motion in the ring plane than in vertical direction. This can be seen in the ratio  $c_z/c_x$  after the scattering, which is several times smaller than the equilibrium value of 0.65. The ratio of the horizontal components  $c_y/c_x$ , however, is close to the equilibrium value of 0.5. Therefore, although the gravitational interaction with the moonlet induces thermal motion in vertical direction, it is negligible compared to the thermal motion induced in the ring plane for moonlets on non-inclined orbits.

Figure 2b shows the x-component of the velocity dispersion, scaled by  $\Omega_0 h$ , at  $\tilde{y} = 0^+$  after the scattering by moonlets with Hill radii of 50m to 500m. For the larger moonlets, with a Hill radius above 100m, the x-component of the velocity dispersion in the gap region, especially the maximal value of  $\tilde{c}_x$ , scales well with the Hill radius of the moonlets.

### 2.3. Hydrodynamic Flow

We describe the ring outside of the scattering region with hydrodynamical equations. Because of the vertically ineffective gravitational scattering of ring particles by the moonlet, we describe the thickness of the ring through the ring temperature, and use vertically averaged balance equations. The mass and momentum balance are given by

$$\frac{\partial \Sigma}{\partial t} + \nabla \cdot (\Sigma \mathbf{u}) = 0 \quad (23)$$

$$\frac{\partial \mathbf{u}}{\partial t} + (\mathbf{u} \cdot \nabla) \mathbf{u} = \mathbf{f} - \frac{1}{\Sigma} \nabla \circ \mathbf{P} . \quad (24)$$

Here  $\Sigma$ ,  $\mathbf{u}$ ,  $\mathbf{f}$  and  $\mathbf{P}$  are the surface mass density, the mean velocity, external volume forces, and the pressure tensor. The pressure tensor is given in Newtonian form

$$\mathbf{P} = p\mathbf{I} - 2\Sigma\nu\mathbf{D} - \Sigma\zeta(\nabla \cdot \mathbf{u})\mathbf{I} , \quad (25)$$

where  $\mathbf{I}$  is the unit tensor. The vertically integrated pressure, kinematic bulk and shear viscosity are denoted by  $p$ ,  $\zeta$  and  $\nu$ . The traceless shear tensor  $\mathbf{D}$  is given by

$$\mathbf{D} = \frac{1}{2} (\nabla \circ \mathbf{u} + \mathbf{u} \circ \nabla) - \frac{1}{3} (\nabla \cdot \mathbf{u})\mathbf{I} , \quad (26)$$

where  $(\nabla \circ \mathbf{u})_{jk} = \nabla_j u_k$  and  $(\mathbf{u} \circ \nabla)_{jk} = \nabla_k u_j$ .

The energy balance of the ring particle's random motion reads

$$\frac{3}{2}\Sigma \left( \frac{\partial T}{\partial t} + (\mathbf{u} \cdot \nabla)T \right) = -\mathbf{P} : \epsilon - \nabla \cdot \mathbf{Q} - \Gamma, \quad (27)$$

where  $T = (c_x^2 + c_y^2 + c_z^2)/3$  is the granular ring temperature and  $\mathbf{Q} = -\kappa_D \nabla T$  the heat flow in the ring with heat conductivity  $\kappa_D$ . The friction term  $\mathbf{P} : \epsilon$  describes the viscous heating of the ring, and  $\Gamma$  accounts for the energy loss due to inelastic collisions.

### 2.3.1. Mass and momentum balance

After the gravitational scattering by the moonlet has opened a gap, the diffusion of the ring particles, described by the nonlinear viscous diffusion equation

$$\frac{\partial \Sigma}{\partial t} + (\Omega(r) - \Omega_0) \frac{\partial \Sigma}{\partial \varphi} - \frac{3}{r} \frac{\partial}{\partial r} \left[ \sqrt{r} \frac{\partial}{\partial r} (\sqrt{r} \nu \Sigma) \right] = 0 \quad (28)$$

for the surface mass density  $\Sigma$ , will smooth out the induced structures (Spahn and Sremčević, 2000; Sremčević, Spahn, and Duschl, 2002).

In order to solve equation (28) we apply the following simplifications, already used by Sremčević, Spahn, and Duschl (2002): Let  $\sigma_1 = \Sigma - \Sigma_0$ , where  $\Sigma_0$  is the equilibrium value of the surface mass density of the unperturbed ring. In the special case of constant kinematic viscosity  $\nu_0$  and without curvature terms, which is consistent with the Hill approximation of the gravitational scattering, equation (28) reduces to a linear partial differential equation

$$K \tilde{x} \frac{\partial \sigma_1}{\partial \varphi} = -\frac{\partial^2 \sigma_1}{\partial \tilde{x}^2}, \quad (29)$$

where the constant  $K$  is defined by

$$K = \frac{\Omega_0 a_0^2}{2\nu_0} \left( \frac{h}{a_0} \right)^3. \quad (30)$$

Equation (29) is point symmetric with respect to the position of the moonlet ( $\tilde{x} = \tilde{y} = \tilde{z} = 0$ ). For the region defined by  $\tilde{x} < 0$  and  $\varphi > 0$ , with boundary

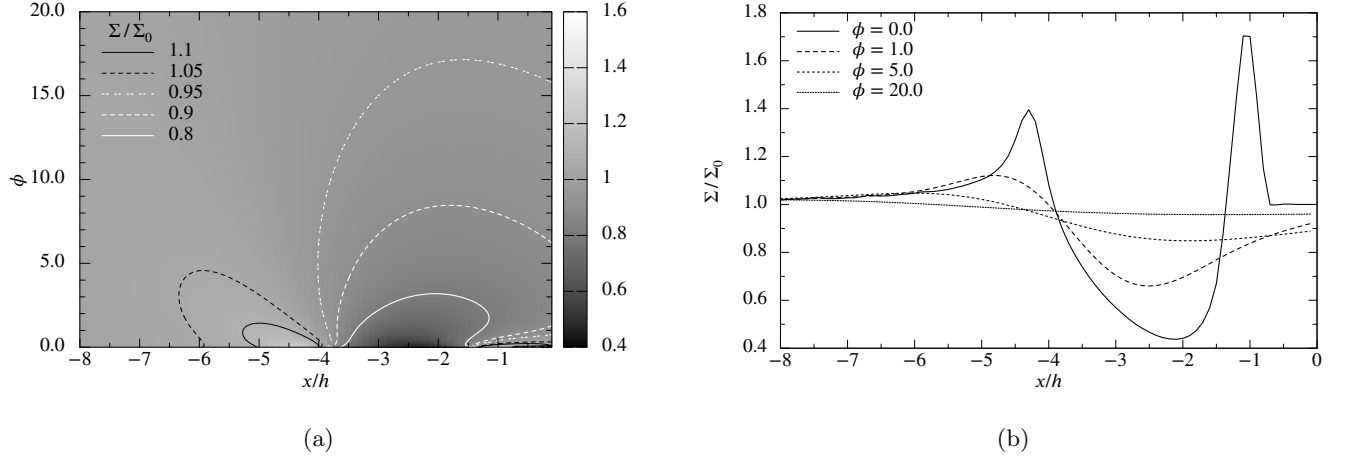


Figure 3: (a) Contour plot of the surface mass density downstream of the moonlet. (b) Surface mass density as a function of  $\tilde{x}$  for different longitudes, illustration the gap-closing. The solid line shows the surface mass density after the scattering by the moonlet.

conditions

$$\sigma_1(\tilde{x} < 0, \varphi = 0^+) = \sigma_{1,\text{ini}} \quad (31)$$

$$\sigma_1(\tilde{x} \rightarrow -\infty, \varphi) = 0 \quad (32)$$

$$\sigma_1(\tilde{x}, \varphi \rightarrow \infty) = 0, \quad (33)$$

Sremčević, Spahn, and Duschl (2002) derived several Greens functions for different constraints at  $\tilde{x} = 0, \varphi > 0$ . The Greens function, which matched their numerical solution best, is an equally weighted superposition of Greens functions for the two cases

$$\sigma_1(\tilde{x} = 0, \varphi) = 0 \quad (34)$$

$$\frac{\partial \sigma_1}{\partial \tilde{x}}(\tilde{x} = 0, \varphi) = 0. \quad (35)$$

We use this Greens function, given by

$$G(\tilde{x}, \phi) = \frac{\sqrt{3}}{2} (-\tilde{x}_0) (3\phi)^{2/3} \exp\left(\frac{\tilde{x}_0^3 + \tilde{x}^3}{9\phi}\right) \text{Bi}\left((3\phi)^{2/3} \tilde{x}_0 \tilde{x}\right), \quad (36)$$

with the scaled azimuth  $\phi = \varphi/K$ , and the Airy function  $\text{Bi}(z)$ , to calculate the surface mass density via

$$\sigma_1(\tilde{x}, \phi) = \int_{-\infty}^0 d\tilde{x}_0 \sigma_{1,\text{ini}}(\tilde{x}_0) G(\tilde{x}, \phi; \tilde{x}_0). \quad (37)$$

As initial surface mass density  $\sigma_{1,\text{ini}}$  we use the vertically integrated mass density calculated with the scattering operator (15), shown in Figure 3b as solid line, and numerically integrate equation (37). The two plots in Figure 3 are again made for a moonlet with 300m Hill radius and the orbital parameters of Earhart. For the value of the kinematic viscosity in Saturn's A ring we used  $\nu_0 = 0.01 \text{ m}^2/\text{s}$  (Tiscareno et al., 2007).

Figure 3a shows the surface mass density after the scattering by the moonlet as function of  $\tilde{x}$  and  $\phi$ . White contour lines represent surface mass density values below  $\Sigma_0$ , showing the evolution of the gap. Black contour lines enclose regions of enhanced surface mass density compared to  $\Sigma_0$ . To illustrate the gap-closing, we plotted the surface mass density as a function of the radial coordinate  $\tilde{x}$  for different longitudes  $\phi$ , shown in Figure 3b.

The azimuthal extent of the surface mass density scales with  $a_0 K$ . Because  $K \propto h^3$ , the importance of the mass diffusion process, in the first few orbits after the scattering by the moonlet, depends strongly on the Hill radius of the moonlet. For large moonlets, e.g.  $h = 500\text{m}$ , the surface mass density stays close to the initial value at  $\phi = 0$ . The smaller the moonlet the larger the influence of the mass diffusion in the first few orbits.

### 2.3.2. Energy balance

In this subsection we will consider the relaxation of the moonlet induced thermal heating by dissipative particle interaction. The vertically ineffective gravitational interaction of ring particles with the moonlet can not explain the vertical height of propeller structures. The moonlet induces thermal motion mainly in lateral direction.

But due to collisions between ring particles, the thermal motion induced in lateral direction will be converted to vertical thermal motion till the ratio  $c_z/c_x$

reaches its local equilibrium value. This asymptotic value of  $c_z/c_x$  is established very fast, after a few collisions per particle (Hämeen-Anttila and Lukkari, 1980; Hämeen-Anttila and Salo, 1993). We therefore use the granular temperature  $T$  to model the evolution of the vertical propeller structure, inferring the thickness of the ring from  $T$  and the equilibrium value of  $c_z/c_x$ .

The thermal energy balance equation in the corotating frame reads

$$\frac{3}{2}\Sigma \left\{ \frac{\partial T}{\partial t} + (\Omega - \Omega_0) \frac{\partial T}{\partial \varphi} + u_r \frac{\partial T}{\partial r} \right\} = -\mathbf{P} : \boldsymbol{\epsilon} - \nabla \cdot \mathbf{Q} - \Gamma \quad . \quad (38)$$

The temperature relaxation of the ring is much slower than the relaxation of the ratio  $c_z/c_x$  to its local equilibrium value. On the other hand, the temperature relaxation is fast compared to the mass diffusion timescale. Therefore we consider, for simplicity, only viscous heating and energy loss due to inelastic collisions. Furthermore, we assume stationarity to obtain

$$\frac{3}{2}(\Omega - \Omega_0) \frac{\partial T}{\partial \varphi} = \frac{9}{4} \nu \Omega_0^2 - k_3 \Omega_0 \tau (1 - \varepsilon^2) T \quad , \quad (39)$$

where we used  $\mathbf{P} : \boldsymbol{\epsilon} = -9\nu\Omega_0^2\Sigma/4$  for the friction term, regarding just the dominant Kepler shear. For the cooling term we used  $\Gamma = k_3\Omega_0\tau(1 - \varepsilon^2)\Sigma T$  with a constant coefficient of restitution  $\varepsilon = 0.5$  and with  $k_3 = 1.5$  (Stewart et al., 1984), corresponding to an energy loss rate

$$\dot{E}_{\text{coll}} = -\omega_c/6(1 - \varepsilon^2)\Sigma c^2 \quad , \quad (40)$$

with collision frequency  $\omega_c = 3\Omega\tau$ , and temperature  $c^2 = 3T$ .

We assume the viscosity to be constant  $\nu = \nu_0$  on timescales which are relevant for the exponential decay of the temperature. With a constant viscosity and a constant coefficient of restitution, viscous heating and collisional cooling balance at a local equilibrium temperature

$$T_{\text{eq}}(\tau) = \frac{9\nu_0\Omega_0}{4k_3(1 - \varepsilon^2)\tau} \quad , \quad (41)$$

which depends on the local optical depth, or assuming equally sized ring particles with particle radius  $R_p$  and mass  $m_p$ , via  $\tau = \pi R_p^2 \Sigma / m_p$ , on the surface mass

density  $\Sigma$ . The temperature of the unperturbed ring before the encounter with the moonlet is  $T_0 = T_{\text{eq}}(\tau_0)$ .

The temperature independent viscosity seems to be a strong restriction and is considered to be a first step towards a more complete description of the problem. The applicability of our model presented in Section 4 will justify the simplifications applied in this work.

With these assumptions equation (39) becomes a linear ordinary differential equation and with  $(\Omega(r) - \Omega_0) \partial/\partial\varphi = -3/2\Omega_0\tilde{x} \partial/\partial\tilde{y}$  and  $T_1 = T - T_0$ :

$$\tilde{x} \frac{\partial T_1}{\partial \tilde{y}} = \nu_0 \Omega_0 \frac{\sigma_1}{\Sigma_0} + \frac{4}{9} k_3 \tau (1 - \varepsilon^2) T_1 . \quad (42)$$

The solution of this equation can be written in the form

$$T_1(\tilde{x}, \tilde{y}) = T_{1,\text{ini}}(\tilde{x}) e^{-\gamma(\tilde{x}, \tilde{y})} + e^{-\gamma(\tilde{x}, \tilde{y})} \int_0^{\tilde{y}} f(\tilde{y}'') e^{\gamma(\tilde{x}, \tilde{y}'')} d\tilde{y}'' , \quad (43)$$

with the functions

$$\begin{aligned} \gamma(\tilde{x}, \tilde{y}) &= \frac{4k_3(1 - \varepsilon^2)\tau_0}{9|\tilde{x}|} \int_0^{\tilde{y}} \frac{\Sigma(\tilde{x}, \tilde{y}')}{\Sigma_0} d\tilde{y}' \\ f(\tilde{x}, \tilde{y}) &= -\frac{\nu_0 \Omega_0}{|\tilde{x}|} \frac{\sigma_1(\tilde{x}, \tilde{y})}{\Sigma_0} . \end{aligned} \quad (44)$$

The plots in Figure 4 show the downstream temperature relaxation. Again they are made for a moonlet with 300m Hill radius and the orbital parameters of Earhart, using  $\nu_0 = 0.01 \text{ m}^2/\text{s}$  as value of the kinematic viscosity in Saturn's A ring. Figure 4a shows a contour plot of the ring temperature  $T$  scaled by the unperturbed ring temperature  $T_0$ , illustrating the azimuthal temperature decay for different radial regions. Ring particles with  $|\tilde{x}| < 0.75$  are on horseshoe orbits and their minimal distance to the moonlet is large, so that there is no considerable thermal excitation. The gap region, on the other hand, is highly excited for quite an azimuthally extended range. Figure 4b shows the azimuthal temperature evolution, at fixed radial position  $\tilde{x} = -2.0$ , downstream from the moonlet. Also, the local equilibrium temperature  $T_{\text{eq}}$  is shown as function of the surface mass density. For the first few orbits, the ring temperature decreases exponentially to the local equilibrium temperature. Afterwards, the viscous

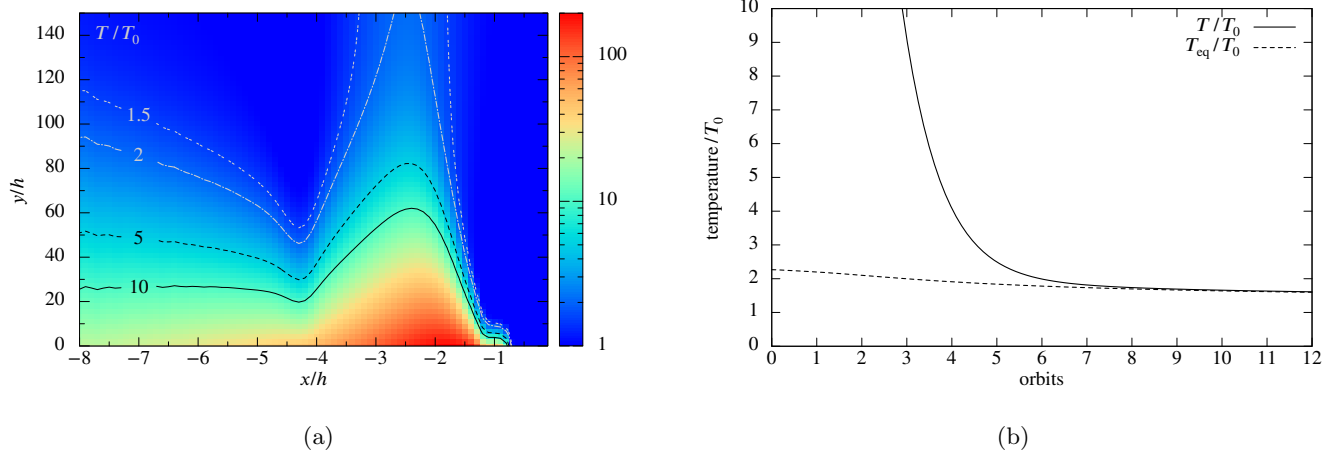


Figure 4: Downstream temperature relaxation for a moonlet with a 300m Hill radius. (a) Contour plot of the temperature decrease downstream of the moonlet. (b) Temperature relaxation at radial position  $\tilde{x} = -2$ . The solid line shows the temperature relaxation of the ring, the dashed line corresponds to the equilibrium temperature  $T_{eq}$ , for which viscous heating and collisional cooling are in balance.

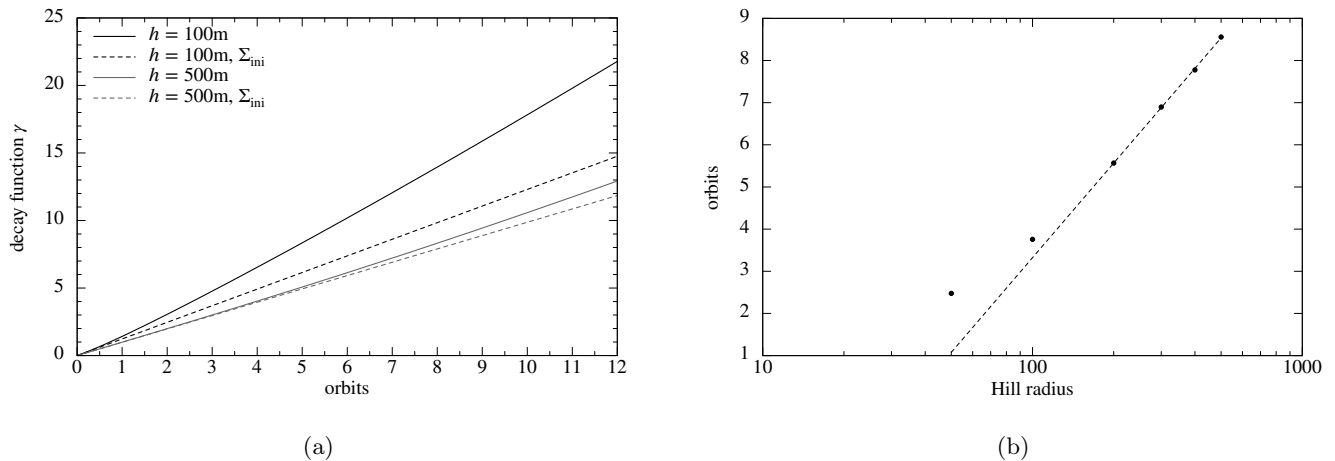


Figure 5: (a) Decay function  $\gamma$  at fixed radial position  $\tilde{x} = -2$  for two moonlets, one with 100m Hill radius and one with 500m Hill radius. The solid lines show  $\gamma$  calculated according to equation (44). In contrast the dashed lines are calculated with an azimuthally constant surface mass density  $\Sigma$  equal to  $\Sigma_{ini}$ . (b) It is shown how many orbits it takes the temperature to decay to 5 percent of  $T_{eq}$  for moonlets with different Hill radii at  $\tilde{x} = -2$ .

heating and the collisional cooling are balanced and the ring temperature evolves as a function of the surface mass density of the ring. In this case the temperature gets within a margin of 5 percent of  $T_{\text{eq}}$  in about 7 orbits.

The influence of the mass diffusion on the temperature decay depends on the Hill radius of the moonlet. Figure 5a shows decay functions  $\gamma$ , calculated at radial position  $\tilde{x} = -2$ , for two moonlets with Hill radii of 100m and 500m. The solid lines show  $\gamma$  calculated according to equation (44). In contrast the dashed lines are calculated with an azimuthally constant surface mass density  $\Sigma$  equal to  $\Sigma_{\text{ini}}$ . For the larger moonlet the solid and the dashed line stay fairly close to each other, because the change of the surface mass density is rather small on the timescale of the exponential decay. For the smaller moonlet both lines differ clearly indicating that the influence of mass diffusion is by far larger.

A fair approximation to the solution (43) is given by

$$T_{\text{approx}}(\tilde{x}, \tilde{y}) = (T_{\text{ini}} - T_{\text{eq}}(\tau)) e^{-\gamma(\tilde{x}, \tilde{y})} + T_{\text{eq}}(\tau) . \quad (45)$$

For  $|\tilde{x}| \geq 1$  the maximal difference of equation (43) to the above approximate solution is about 5 percent, tested for moonlets with Hill radii of 50m to 500m.

The exponential decay of the temperature stops after a few orbits, when the local equilibrium temperature  $T_{\text{eq}}$  is reached. Figure 5b sketches how many orbits it takes to get within 5 percent of  $T_{\text{eq}}$  for moonlets with different Hill radii at fixed radial position  $\tilde{x} = -2$ . Using the approximate solution  $T_{\text{approx}}$ , the azimuthal position  $\tilde{y}_\xi$  where the the ratio  $T/T_{\text{eq}}$  equals  $1 + \xi$  is

$$\tilde{y}_\xi = \frac{1}{\langle \gamma \rangle} \ln \left( \frac{T_{\text{ini}} - T_{\text{eq}}(\tau)}{\xi T_{\text{eq}}(\tau)} \right) , \quad (46)$$

where we defined formally  $\gamma(\tilde{x}, \tilde{y}) = \langle \gamma \rangle \tilde{y}_\xi$ . Both  $\langle \gamma \rangle$  and  $T_{\text{eq}}$  depend on the optical depth  $\tau$  and therefore on the azimuthal position  $\tilde{y}$ . For large moonlets, close in size to ring-moons able to open a circumferential gap,  $\tau$  is nearly constant on the timescale of the exponential temperature decay. Because of  $T_{\text{ini}} \gg T_{\text{eq}}$  and  $T_{\text{ini}} \propto h^2$  for large moonlets,  $\tilde{y}_\xi$  will scale with  $\tilde{y}_\xi \propto 2 \ln(h)$ . In Figure 5b a fit of the function  $\tilde{y}_\xi = A \ln(Bh^2)$  to the values of the large moonlets with Hill radii of 200m to 500m is presented in order to underline this

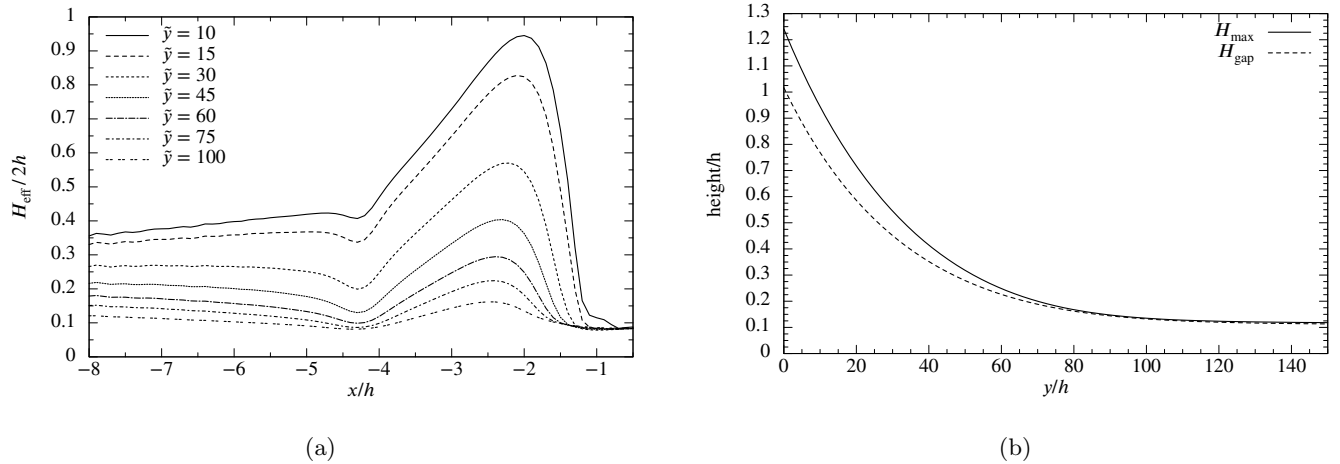


Figure 6: Azimuthal relaxation of the propeller height for a moonlet with 300m Hill radius. (a) Propeller heights as function of radial coordinate  $\tilde{x}$  for different longitudes. (b) Downstream relaxation of the propeller height. The solid line shows the relaxation at  $\tilde{x} = -2$ . The dashed line shows the propeller height radially averaged over the gap region.

scaling.

### 3. The vertical height of propellers

In the thin-disk approximation and with a  $z$  independent vertical velocity dispersion  $c_z$ , the vertical profile of the mass density can be described well by a Gaussian with standard deviation  $c_z/\Omega_0$  (Stewart et al., 1984; Simon and Jenkins, 1994; Schmidt et al., 1999). We use the effective geometric thickness  $H_{\text{eff}}$  as a measure of the ring thickness and determine the height of the propeller structure as half the effective geometric thickness of the ring.

To determine  $c_z$  as a function of the temperature  $T$ , we use the equilibrium values of the ratios  $c_z/c_x$  and  $c_y/c_x$ . A perturbed ring will reach the equilibrium values of these quantities after a few collisions per particle (Hämeen-Anttila and Lukkari, 1980; Hämeen-Anttila and Salo, 1993). In Saturn's A ring with  $\tau = 0.5$  and with a collision frequency of  $\omega_c = 3\Omega\tau$ , there are about 10 collisions per particle per orbit. We assume that after 5 collisions, corresponding to half an

$h/m$	50	100	200	300	400	500
$H_{\max}/h$	0.90	0.90	0.94	0.95	0.95	0.96
$H_{\text{gap}}/h$	0.80	0.72	0.72	0.73	0.73	0.74

Table 1: Heights for moonlets with different Hill radii from 50m to 500m.  $H_{\max}$  is the height at  $\tilde{x} = -2.0$  and  $\tilde{y} = 10$ .  $H_{\text{gap}}$  is the height averaged over the gap region at azimuthal position  $\tilde{y} = 12$ .

orbit, the equilibrium values of these ratios are established. With the relaxed ratios  $(c_z/c_x)_{\text{eq}} = 0.65$  and  $(c_y/c_x)_{\text{eq}} = 0.5$ , the z component of the velocity dispersion in terms of  $T$  is given by

$$c_z(T) = \left(\frac{c_z}{c_x}\right)_{\text{eq}} \sqrt{\frac{3T}{1 + (c_y/c_x)_{\text{eq}}^2 + (c_z/c_x)_{\text{eq}}^2}}. \quad (47)$$

The two plots in Figure 6 are made using the same parameters as were taken for Figure 4, i.e. a moonlet with 300m Hill radius, the orbital parameters of Earhart and a kinematic viscosity of  $\nu_0 = 0.01 \text{ m}^2/\text{s}$ . In Figure 6a, the height of the propeller structure as a function of the radial coordinate  $\tilde{x}$  is plotted for different values of  $\tilde{y}$ . The largest heights are reached in the region between  $\tilde{x} = -4$  and  $\tilde{x} = -1$ , the maximum being at about  $\tilde{x} = -2$  for  $\tilde{y} = 10$  and slowly moving to  $\tilde{x} = -2.5$  at  $\tilde{y} = 100$ .

The azimuthal relaxation of the height of the propeller structure, for  $\tilde{x} = -2$ , is shown in Figure 6b. We assume that after half an orbit or 5 collisions per particle the equilibrium value of  $c_z/c_x$  is established and that afterwards the ring temperature describes the propeller height well. At radial position  $\tilde{x} = -2$ , half an orbit corresponds approximately to  $\tilde{y} = 10$ . The height at  $\tilde{y} = 10$  is 0.95 Hill radii or about 285m.

Furthermore, Figure 6b sketches the propeller height radially averaged over the gap region. We choose the approximate middle of the gap at  $\tilde{x} = -2.5$  as a reference, and in that case half an orbit corresponds to  $\tilde{y} = 12$ . At that position the gap averaged propeller height is 0.72 Hill radii or about 215m.

Table 1 shows propeller heights for moonlets with different Hill radii.  $H_{\max}$  is the height at radial position  $\tilde{x} = -2$  and azimuthal position  $\tilde{y} = 10$ .  $H_{\text{gap}}$  is the height averaged over the gap region at azimuthal position  $\tilde{y} = 12$ . The maximal heights are close to one Hill radius for the tested moonlet sizes. The values of the gap averaged height for the moonlets with Hill radius 100m and above are approximately 0.7 Hill radii. The averaged propeller height for the moonlet with a 50m Hill radius is larger (0.8h), which is due to the large value of the unperturbed height of the ring scaled by the Hill radius of the moonlet.

#### 4. Discussion

We study the vertical extent of propeller structures in Saturn’s rings, focusing on the propeller gap region. The effective geometric thickness  $H_{\text{eff}}$  is used to describe the propeller height as a function of the ring temperature, calculated using the equilibrium ratios of the thermal velocities. A vertically constant ring temperature serves as a fair assumption, because for the low optical depths in the propeller gap region the vertical dependence of the ring temperature is rather weak (Schmidt et al., 1999).

In our model the azimuthal temperature decrease is caused dominantly by the disturbed balance of viscous heating and collisional cooling. We assume a constant coefficient of restitution for the cooling term and constant viscosity for the viscous heating term. This is a simplification, but allows a semi-analytical solution of the azimuthal temperature relaxation (some integrals have to be numerically evaluated), and most important, it is consistent with images of propeller shadows taken by the Cassini spacecraft.

The restriction of a constant  $\nu_0$  could be dropped by introducing e.g. a power law dependence (Spahn et al., 2000),

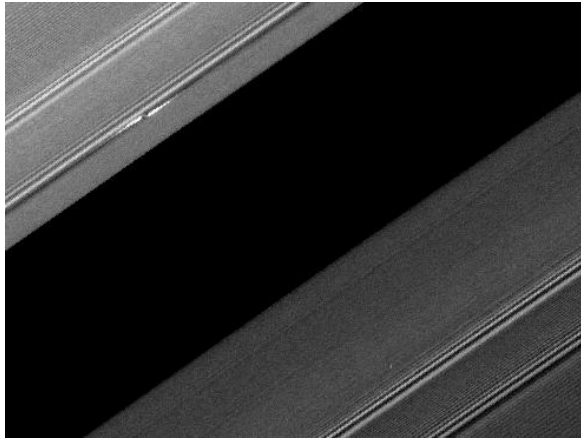
$$\nu = \nu_0 \left( \frac{\Sigma}{\Sigma_0} \right)^\beta \left( \frac{r}{a_0} \right)^\gamma \left( \frac{T}{T_0} \right)^\alpha . \quad (48)$$

For small moonlets ( $h \leq 50\text{m}$ ) one has a rather small ratio  $T_{\text{ini}}/T_0 \leq 5$ . The power law dependence (48) with  $\alpha = 1/2$  (Salo et al., 2001) then gives a viscosity

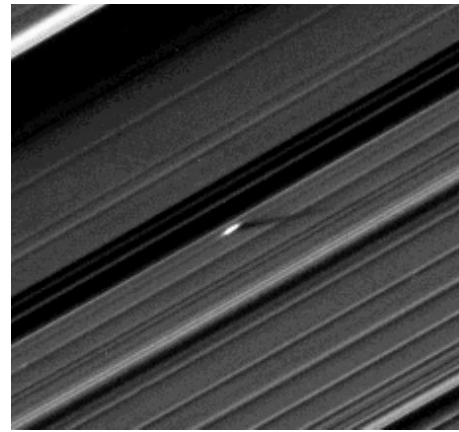
about twice as large as the unperturbed one. On the other hand, the surface mass density in the gap region after the scattering by the moonlet is about half of the unperturbed value, so that a constant viscosity  $\nu_0$  can be justified. In case of large moonlets the ratio  $T_{\text{ini}}/T_0$  is by far higher (190 for a moonlet with 300m Hill radius at  $|\tilde{x}| = 2$ ). The viscosity will rise considerably with increasing temperature, tending to an increased heating, and thus, to an increased cooling time scale. However, because of an increasing coefficient of restitution and due to increased collision rates, an enhanced cooling works against that effect. Insofar, as a first step, we have used a constant viscosity and a constant coefficient of restitution, interpreting both as effective values.

Furthermore, we have neglected the temperature decrease due to heat conduction, based on the grounds that the relaxation of the ring temperature by granular cooling is the faster process, compared to the large diffusive time scales blurring the propeller gaps. However, heat conduction as well as viscous diffusion could become important for small moonlets. We have estimated the temperature decrease due to heat conduction for a simplified model, described in Appendix A. For small moonlets ( $h \leq 50\text{m}$ ) the temperature decrease due to heat conduction is comparable to the temperature decrease of our granular cooling driven solution (43). On the other hand, for large moonlets the temperature decrease due to heat conduction was approximately 20 times smaller than our cooling driven relaxation after 10 orbits, justifying a neglect of heat conduction for large moonlets, and thus, our approach.

In the summer of 2009, near Saturn’s equinox, the Cassini spacecraft took images, which show prominent shadows cast by propeller moonlets. The height of the propeller features were calculated from the observed shadow length (Tiscareno et al., 2010). For the propeller moonlet Blériot, a height of  $430 \pm 30\text{m}$  was determined, for Santos-Dumont 120m, and for Earhart 260m. Figure 7 shows the propeller moonlet Earhart orbiting near the Encke gap, where Figure 7b portrays Earhart in August 2009, a few days after Saturn’s equinox, to cast a 350km long shadow. In contrast, Figure 7a shows Earhart in April 2008 long before equinox.



(a)



(b)

Figure 7: The propeller moonlet Earhart near the Enke gap. (a) This image was taken by the Cassini spacecraft on April 11, 2008 with Cassini's narrow angle camera. The resolution is about 2 km per pixel. The propeller structure is about 5 km in radial dimension and about 60 km in azimuthal dimension. (b) Image of Earhart near Saturn's equinox, taken by Cassini's narrow angle camera on August 13, 2009. The resolution is 7 km/pixel. The shadow cast by the propeller is 350km long and the height of the propeller is estimated to be 260m (Tiscareno et al., 2010). Credit: NASA/JPL/Space Science Institute

Using our values of the gap averaged propeller height from Table 1, the height of the propeller structure is approximately 0.7 times the Hill radius of the propeller moonlet. This gives 370m for the Hill radius of Earhart and 615m for the Hill radius of Blériot. Assuming a spherical shape, the moonlet radius of Earhart is then 240m for a mass density of  $600 \text{ kg/m}^3$ , and 280m for a mass density of  $400 \text{ kg/m}^3$ .

We determined the azimuthal extent of Earhart from Figure 7b to be  $120 \pm 20 \text{ km}$ , the Cassini ISS team reported about 130km on their website. The propeller structure thus azimuthally extends about  $60 \pm 10 \text{ km}$  downstream from the moonlet. In Section 2.3.2 we used a ring temperature of  $1.05 \cdot T_{\text{eq}}$  to determine the end of the exponential temperature decay. Using this criterium for a moonlet with 370m Hill radius and for the radial ring particle position  $|\tilde{x}| = 2.5$  (approximately the middle of the gap region), the exponential temperature decay stops after about 7 orbits. These 7 orbits at  $|\tilde{x}| = 2.5$  corresponds to an azimuthal propeller length of 61km downstream of the moonlet which agrees astonishingly well with the  $60 \pm 10 \text{ km}$  determined from Figure 7b. To calculate the mean decay constant  $\langle \gamma \rangle$ , we used equation (46) with the determined azimuthal propeller extent, to find  $\langle \gamma \rangle = 0.05$ . At  $|\tilde{x}| = 2.5$  this corresponds to  $k_3(1 - \varepsilon^2) = 1.1$ , which nicely compares to  $k_3(1 - \varepsilon^2) = 1.125$  used in our model.

## 5. Summary and Outlook

In the present work we study the vertical extent of propeller structures in Saturn's rings. Our focus lies on the gap region of the propeller and on non-inclined propeller moonlets. In order to describe the vertical structure of propellers we extend the model of Spahn and Sremčević (2000) to include the vertical direction. We use the scattering operator concept (Spahn and Wiebicke, 1989) to model the gravitational interaction of the embedded moonlet with the ring particles, taking place in a relatively small region around the moonlet. Outside this region we describe the Keplerian ring flow using hydrodynamic equations. The azimuthal relaxation of the propeller height is modelled by the disturbed bal-

ance of viscous heating and granular cooling using the energy balance equation of the ring particle's thermal motion.

Our conclusions and results are:

1. Considering only the gravitational interaction of ring particles with a non-inclined moonlet, the moonlet does not induce considerable vertical excursions of ring particles. However, the moonlet causes considerable thermal motion in the ring plane. The maximal value of this thermal motion, when measured by the radial thermal velocity, scales well with the Hill radius according to  $c_x \sim h\Omega$ .
2. Collisions between ring particles are an effective mechanism to locally convert the lateral induced thermal motion into vertical excursions of ring particles. After the scattering by the moonlet, the ratio of vertical to radial thermal velocity is far from its equilibrium value, but the local relaxation to the equilibrium value takes only a few collisions per particle (Hämeen-Anttila and Lukkari, 1980; Hämeen-Anttila and Salo, 1993). Consequently, after a few collisions per particle, the ring temperature describes the vertical extent of the propeller structure astonishingly well.
3. We use half of the effective geometric thickness of the ring as a measure for the propeller height in the gap region and find maximal heights on the order of the Hill radius of the moonlet. The height, averaged over the gap region, is obtained to be about 0.7 Hill radii.
4. For the first few orbits, the azimuthal evolution of the ring temperature is characterised by an exponential decay to a local equilibrium temperature. Later, the viscous heating and the collisional cooling are balanced and the ring temperature evolves as a function of the local optical depth of the ring. The fast decay is consistent with images of Earhart, taken by the Cassini spacecraft near Saturn's equinox. We found that for the exponential decay phase the neglect of heat conduction is a useful and valid assumption for large propeller moonlets like Blériot and Earhart. For small moonlets, e.g. with Hill radius of 50m, heat conduction and dissipative effects become

important right after the scattering.

Future work should incorporate a kinetic description of the counteracting viscous heating and collisional cooling, to study the consequences of a velocity dependent coefficient of restitution and a temperature dependent viscosity on the azimuthal relaxation of the ring temperature.

Another subject of ongoing work is the vertical extent of the wake region of propellers. By dropping the averaging process in the calculation of the scattering operator, radial and vertical phase information of the ring particle’s motion is preserved. This allows us to describe the coherent motion of ring particles in the wake region. An extension to inclined moonlets would then allow comparison to the wake region of the ring-moon Daphnis.

Further work should be done on the inclusion of heat conduction, viscous diffusion and fluctuations into our model, to better describe propellers of small moonlets. Finally, we plan to compare our results to direct N-body simulations of propellers (Seiß et al., 2005; Sremčević et al., 2007).

### Acknowledgements

We thank Heikki Salo for very useful discussions. We kindly acknowledge the efforts of the Cassini ISS team in the design and operation of the ISS instrument. This work was supported by Deutsche Forschungsgemeinschaft (Sp 384/24-1; 25-1).

### Appendix A. Influence of heat conduction on the temperature decay

We neglected the heat conduction term in equation (39) on the grounds that the relaxation of the ring temperature is, compared to the mass diffusion, a fast process. To check for which parameters this assumption is valid, we use our solution of (39) to estimate how large a heat conduction term in equation (42) would have been. With a heat conduction term, equation (42) reads

$$\tilde{x} \frac{\partial T_1}{\partial \tilde{y}} = \nu_0 \Omega_0 \frac{\sigma_1}{\Sigma_0} + \frac{4}{9} k_3 \tau (1 - \varepsilon^2) T_1 - \frac{4\kappa}{9\Omega_0 h^2} \left( \frac{\partial^2 T_1}{\partial \tilde{x}^2} + \frac{\partial^2 T_1}{\partial \tilde{y}^2} \right), \quad (\text{A.1})$$

with the kinematic heat conductivity  $\kappa$ , which we assumed to be constant. Further we assume  $\kappa/\nu \approx 20$  (Salo et al., 2001). The azimuthal part of the heat conduction term is several times smaller than the cooling term which describes the inelastic collision between ring particles. For a moonlet with 50m Hill radius, it is at least 20 times smaller, whereas it is at least two orders of magnitude smaller for a moonlet with 200m Hill radius. The radial part of the heat conduction term, on the other hand, is of the order of the cooling term for  $|\tilde{x}| < 1.5$ . For small moonlets, e.g.  $h = 50\text{m}$ , this applies also for  $|\tilde{x}| < 4$ .

On the timescale of the mass diffusion process, heat conduction can not be neglected, but for small moonlets heat conduction seems to be also important in the first few orbits. Therefore, we estimated the temperature decrease in the middle of the gap at  $\tilde{x} = -2.5$ . For that, we assumed a Gaussian radial temperature profile at  $\tilde{y} = 0^+$ , centered at  $\tilde{x}_0 = -2.5$  and with standard deviation  $\sigma$  calculated according to full width at half maximum of 3:

$$T(\tilde{x}, 0) = T(\tilde{x}_0, 0) \exp\left(-\frac{(\tilde{x} - \tilde{x}_0)^2}{2\sigma^2}\right). \quad (\text{A.2})$$

Using this as initial condition, we solved equation (A.1) neglecting all but the heat conduction term

$$\tilde{x}_0 \frac{\partial T_1}{\partial \tilde{y}} = -\frac{4\kappa}{9\Omega_0 h^2} \left( \frac{\partial^2 T_1}{\partial \tilde{x}^2} + \frac{\partial^2 T_1}{\partial \tilde{y}^2} \right), \quad (\text{A.3})$$

further simplified by setting  $\tilde{x} = \tilde{x}_0$ . The azimuthal evolution of the temperature at radial position  $\tilde{x}_0$  is then given by

$$T(\tilde{x}_0, \tilde{y}) = \sqrt{2\pi\sigma^2} T(\tilde{x}_0, 0) \left( 2\pi\sigma^2 + \frac{16\pi\kappa}{9\Omega_0 h^2 \tilde{x}_0} \tilde{y} \right)^{-1/2}. \quad (\text{A.4})$$

For a moonlet with a Hill radius of 50m, the temperature decrease according to the above solution was approximately equal to the temperature decrease of our solution (43) in the first few orbits. For a moonlet with 200m Hill radius on the other hand, the temperature decrease due to heat conduction after 10 orbits was approximately 20 times smaller than the temperature decrease of our solution (43). This indicates, although we neglected the Kepler shear by setting  $\tilde{x} = \tilde{x}_0$  in equation (A.3), the importance of heat conduction for the temperature decay

for small moonlets. For large moonlets, 200m Hill radius and above, the neglect of heat conduction seems to be a valid assumption.

## References

- Araki, S., Tremaine, S., 1986, The Dynamics of Dense Particle Disks, *Icarus*, vol. 65, pp.83-109.
- Artymowicz, P., 2006, Planetary Systems, Am. Inst. Physics Conf. Series, vol. 843, pp.3-34.
- Borderies, N., Goldreich, P., Tremaine, S., 1985, A Granular Flow Model for Dense Planetary Rings, *Icarus*, vol. 63, pp.406-420.
- Burns, J.A. and Cuzzi, J.N.C., 2006, Our local astrophysical laboratory, *Science*, vol. 312, pp.1753-1755.
- Goldreich, P. and Tremaine, S., 1978, Saturn's rings velocity dispersion, *Icarus*, vol. 34, pp.227-239.
- Hämeen-Anttila, K. A. and Lukkari, J., 1980, Numerical simulations of collisions in Keplerian systems, *A&AA*, vol. 71, pp. 475-497.
- Hämeen-Anttila, K. A. and Salo, H., 1993, Generalized Theory of Impacts in Particulate Systems, *EM&P*, vol. 62, pp. 47-84.
- Hénon, M. and Petit, J.-M., 1986, Series expansion for encounter-type solutions of Hill's problem, *Celestial Mechanics*, vol. 38, pp. 67-100.
- Hill, G.W., 1878, Researches in the Lunar Theory, *Am. J. Math*, vol. 1, pp. 5-26, 129-147, 245-260.
- Ida, S., Makino, J., 1992, N-body simulation of gravitational interaction between planetesimals and a protoplanet. I - Velocity distribution of planetesimals, *Icarus*, vol. 96, pp. 107-120.

- Jacobson R. A. et al., 2008, Revised orbits of Saturn's small inner satellites, *AJ*, vol. 135, pp. 261-263.
- Lewis, M. C., Stewart, G. R., 2000, Collisional dynamics of perturbed planetary rings I, *AJ*, vol. 120, pp.3295-3310.
- Lewis, M. C., Stewart, G. R., 2009, Features around embedded moonlets in Saturn's rings: The role of self-gravity and particle size distributions, *Icarus*, vol. 199, pp.387-412.
- Lissauer, J.J., 1993, Planet formation, *ARA&A*, vol. 31, pp. 129-174.
- Ohtsuki, K., Emori, H., 2000, Local N-Body Simulations for the Distribution and Evolution of Particle Velocities in Planetary Rings, *AJ*, vol. 119, pp. 403-416.
- Papaloizou, J.C.B. et al. 2007, Disk-Planet Interactions During Planet Formation, *Protostars and Planets V*, pp. 655-668.
- Petit, J.-M., Hénon, M., 1986, Satellite encounters, *Icarus*, vol. 66, pp. 536-555.
- Petit, J.-M., Hénon, M., 1987, A numerical simulation of planetary rings. I – Binary encounters, *A&A*, vol. 173, pp. 389-404.
- Press, W. H., Teukolsky, S. A., Vetterling, W. T., Flannery, B. P., 1992, *Numerical Recipes in C* (2nd ed.), Cambridge University Press.
- Salo, H., 1991, Numerical Simulations of Dense Collisional Systems, *Icarus*, vol. 90, pp. 254-270.
- Salo, H., Schmidt, J., Spahn, F., 2001, Viscous Overstability in Saturn's B Ring. I. Direct Simulations and Measurement of Transport Coefficients, *Icarus*, vol. 153, pp. 295-315.
- Schmidt, J., Salo, H., Petzschmann, O., Spahn, F., 1999, Vertical distribution of temperature and density in a planetary ring, *A&A*, vol. 345, pp. 646-652.

- Seiß, M., Spahn, F., Sremčević, M., Salo, H., 2005, Structures induced by small moonlets in Saturn's rings: Implications for the Cassini mission, *Geophys. Res. Lett.*, vol. 32, doi:10.1029/2005GL022506.
- Showalter, M. R., Cuzzi, J. N., Marouf, E. A., Esposito, L. W., 1986, Satellite "Wakes" and the Orbit of the Encke Gap Moonlet, *Icarus*, vol. 66, pp. 297-323.
- Simon, V., Jenkins, J. T., 1994, On the Vertical Structure of Dilute Planetary Rings, *Icarus*, vol. 110, pp. 109-116.
- Spahn, F., 1987, Scattering Properties of a Moonlet (Satellite) Embedded in a Particle Ring: Application to the Rings of Saturn, *Icarus*, vol. 71, pp. 69-77.
- Spahn, F., Wiebicke, H. J., 1989, Long-Term Gravitational Influence of Moonlets in Planetary Rings, *Icarus*, vol. 77, pp. 124-134.
- Spahn, F., Scholl, H., Hertzsch, J.-M., 1994, Structures in planetary rings caused by embedded moonlets, *Icarus*, vol. 111, pp. 514-535.
- Spahn, F., Sremčević, M., 2000, Density patterns induced by small moonlets in Saturn's rings?, *A&A*, vol. 358, pp. 368-372.
- Spahn, F., Schmidt, J., Petzschmann, O., Salo, H., 2000, Note: Stability analysis of a Keplerian disk of granular grains: Influence of thermal diffusion, *Icarus*, vol. 145, pp. 657-660.
- Sremčević, M., Spahn, F., Duschl, W.J., 2002, Density structures in perturbed thin cold discs, *Mon. Not. R. Astron. Soc.*, vol. 337, 1139-1152.
- Sremčević, M., Schmidt, J., Salo, H., Seiß, M., Spahn, F., Albers, N., 2007, A belt of moonlets in Saturn's A ring, *Nature*, vol. 449, 1019-1021.
- Stewart, G. R., Lin, D. N. C., Bodenheimer, P., 1984, Collision-induced transport processes in planetary rings. In *Planetary Rings* (R. Greenberg and A. Brahic, Eds.), pp. 447-512, Univ. of Arizona Press, Tucson.

- Tiscareno, M. S., Burns, J. A., Hedman, M. M., Porco, C. C., Weiss, J. W., Murray, C. D., and Dones, L., 2006, Observation of “propellers” indicates 100-metre diameter moonlets reside in Saturn’s A-ring. *Nature*, vol. 440, pp. 648-652.
- Tiscareno, M. S. et al., 2007, Cassini imaging of Saturn’s rings. II. A wavelet technique for analysis of density waves and other radial structure in the rings, *Icarus*, vol. 189, pp. 14-34.
- Tiscareno, M. S., Burns, J. A., Hedman, M. M.; Porco, C. C., 2008, The Population of Propellers in Saturn’s A Ring, *Astronomical Journal*, vol. 135, pp. 1083-1091.
- Tiscareno M. S. et al., 2010, Physical Characteristics and Non-Keplerian Orbital Motion of “Propeller” Moons Embedded in Saturn’s Rings, *ApJL*, vol. 718, pp. L92-L96.
- Weiss, J. W., Porco, C. C., Tiscareno M. S., 2009, Ring Edge Waves and the Masses of Nearby Satellites, *Astronomical Journal*, vol. 138, pp. 272-286.